High-Resolution Cellular MRI: Gadolinium and Iron Oxide Nanoparticles for in-Depth Dual-Cell Imaging of Engineered Tissue Constructs

Riccardo Di Corato,[†] Florence Gazeau,[†] Catherine Le Visage,[‡] Delphine Fayol,[†] Pierre Levitz,[§] François Lux,[⊥] Didier Letourneur,[‡] Nathalie Luciani,[†] Olivier Tillement,[⊥] and Claire Wilhelm[†,*]

[†]Laboratoire Matière et Systèmes Complexes, UMR 7057, CNRS and Université Paris Diderot, France, [‡]Inserm, U698, Bio-ingénierie Cardiovasculaire, Université Paris Diderot, CHU X. Bichat, Paris, France, [§]Laboratoire de Physique de la Matière Condensée (PMC), UMR 7643 CNRS/Ecole Polytechnique, France, and [⊥]Laboratoire de Physico-Chimie des Matériaux Luminescents, UMR 5620 CNRS—Université Claude Bernard Lyon 1, France

ABSTRACT Recent advances in cell therapy and tissue engineering opened new windows for regenerative medicine, but still necessitate innovative noninvasive imaging technologies. We demonstrate that high-resolution magnetic resonance imaging (MRI) allows combining cellular-scale resolution with the ability to detect two cell types simultaneously at any tissue depth. Two contrast agents, based on iron oxide and gadolinium oxide rigid nanoplatforms, were used to "tattoo" endothelial cells and stem cells, respectively, with no impact on cell functions, including their capacity for differentiation. The labeled cells' contrast properties were optimized for simultaneous MRI detection: endothelial cells and stem cells seeded together in a polysaccharide-based scaffold material for tissue engineering appeared respectively in black and white and could be tracked, at the cellular level, both *in vitro* and *in vivo*. In addition, endothelial cells labeled with iron oxide nanoparticles could be remotely manipulated by applying a magnetic field, allowing the creation of vessel substitutes with in-depth detection of individual cellular components.

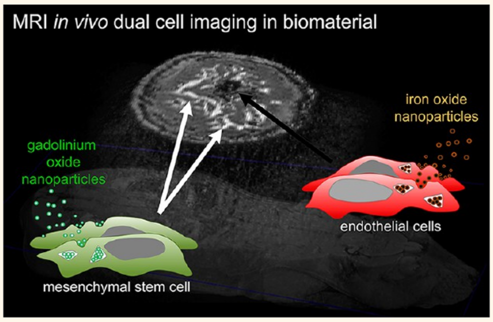

KEYWORDS: nanobiotechnology · magnetic resonance imaging · biomaterials · tissue engineering · stem cells

By combining biomaterials with living cells, tissue engineering is seeking to create biological grafts with specific features of native tissues, opening up new perspectives for tissue repair.[1−3] Direct injection of therapeutic cells is another promising approach for tissue reconstruction.[4] However, one obstacle to the development of such therapies is that current imaging techniques cannot visualize the fate of implanted cells deep within the body. Recent advances in nonlinear microscopy have led to new strategies for observation of living biological tissues,[5,6] but such approaches are still restricted in depth. Advances in magnetic resonance imaging (MRI),[7] scintigraphy,[8] and fluorescence-based methods[9] have taken *in vivo* imaging to a new level, by revealing the fate and functioning of cells. Optical methods for tracking cells tagged with fluorescent or luminescent labels are being developed for preclinical small animal studies,[10] but these are also limited to a depth of a few millimeters, severely hindering their clinical application. Radiolabeled cells can be detected *in vivo* by means of positron emission tomography (PET), with excellent sensitivity and tissue penetration, but with insufficient spatial resolution or anatomic images, while the use of radioactive tracers raises safety issues. In contrast, MRI is a nonradiative and noninvasive method suitable for longitudinal studies, providing anatomic images at any depth with excellent spatial resolution. To detect cells by MRI, the cells of interest must first be tagged with a contrast agent. The current approach is to use superparamagnetic iron oxide nanoparticles (IONPs),[11,12] which, by reducing the T_2 relaxation time, lead to a loss of signal; IONPs are therefore known as negative contrast agents. Many studies of IONP biocompatibility have been published in recent years, showing that

* Address correspondence to claire.wilhelm@univ-paris-diderot.fr.

Received for review February 18, 2013 and accepted August 7, 2013.

10.1021/nn401095p

these nanomaterials have an extremely low impact on cell functions. With the advent of high-resolution MRI, individual cells can now be visualized in black on T_2-weighted images (see ref 13 for a review). However, few studies have achieved cellular MRI imaging in biomaterials for the purposes of tissue engineering.[14−17] IONP-labeled cells also have another property of particular interest to tissue engineering, namely, their capacity for remote magnetic manipulation, paving the way for the creation of organized cell assemblies.[18,19] To our knowledge, the combination of a magnetically organized pattern with high-resolution MRI imaging has not previously been demonstrated.

Currently, the main limitation of cellular MRI is the lack of a multicellular imaging method, which is crucial to monitor multicellular grafts within their host tissue. Paramagnetic gadolinium (Gd) derivatives are another type of MRI contrast agent. These "positive" contrast agents reduce the T_1 relaxation time, thereby enhancing the MRI signal. Although Gd chelates are already extensively used in the clinic to detect lesions or visualize vessels,[20] only rare attempts have been made to exploit their properties for cellular imaging as gadolinium compounds[21−25] or in combination with T_2 agents for concurrent dual contrast.[26] In this context, Gd-labeled cells have never been detected at a cell resolution by T_1-weighted MRI. Among the candidates for a cellular paramagnetic label, gadolinium-based nanoparticles (GdNP) offer the advantages of efficient intracellular labeling and minimal toxicity.[27]

The method described here uses dual T_1 (GdNP) and T_2 (IONP) cell labels to image stem cells and endothelial cells simultaneously within a biomaterial used for tissue engineering, by means of high-resolution MRI. The use of endothelial cells and stem cells was motivated by the common need to vascularize reconstructed tissues, which is crucial for cell survival, nutrient transport, and waste removal.[28] A promising approach is to seed scaffolds with two cell types: stem cells or specific cells of the targeted organ combined with endothelial cells or progenitors capable of facilitating *in situ* formation of blood vessels.[29]

After studying IONP and GdNP incorporation in endothelial cells and stem cells at various extracellular concentrations, we examined their impact on cell functions (especially differentiation capacity) and their contrast properties. Optimization of both cell seeding in biomaterials and imaging protocol provided high-resolution images of a multicellular construct with stem cells depicted in white and endothelial cells in black.

Still, it is important to emphasize that the MRI parameters used (specifically the gradient echo time and repetition time) are the key factors for detecting T_1 and T_2 signals exclusively. Indeed, IONP and GdNP shorten both the T_1 and T_2 relaxation times, differing only by the relative shortening of each parameter (the T_1/T_2 ratio is much higher for GdNP than for IONP). It is the optimization of the sequence parameters that allows simultaneous detection of the two agents (hypo- *versus* hypersignal) on the same image.

Moreover, dual cell tracking could be performed, *in vivo*, for two weeks. Finally, a tubular template of the same biomaterial was used to create a cellular graft with a structure mimicking that of a blood vessel, thanks to a magnetic patterning of the endothelium. MRI images confirmed the dual imaging of both the muscle layer in white and the endothelium in black.

RESULTS

The aim of this study is to combine cellular-scale resolution with the ability to detect several cell types simultaneously at any tissue depth within a living body. The schematic of such cell-engineered tissue imaging is proposed in Figure 1.

Nanotagging of Endothelial and Stem Cells. The IONPs used here were maghemite nanoparticles with a diameter of 7 nm and a negatively charged surface (Figure 2a). They have already proved to be extremely effective agents for *in vitro* magnetic labeling of all cell types tested so far (cells from different species; primary cultures and cell lines; immune, cancer, muscle, endothelial, and stem cells).[30]

GdNP have been less extensively studied as cell labels. They are composed of a polysiloxane network bearing chelating species, *e.g.*, DTPA (diethylenetriaminepentaacetic acid), at the surface. These particles display a size of about 1−3 nm (and an associated mass ranging from 3 to 10 kDa). They have already proven *in vivo* their efficiency as a multimodal theranostic contrast agent for MRI and radiosensitization.[31] However, their possible functional impact on therapeutic cells (stem cell differentiation for example) remains to be determined.

To tune the cellular capture of these GdNPs, two types of nanoparticles were synthetized ($GdNP_1$ and $GdNP_2$, Figure 2a) according to different protocols. First, $GdNP_1$ comprises a fluorescent FITC group. Second, the synthesis led to two different sizes (3−4 and 1−2 nm for $GdNP_1$ and $GdNP_2$, respectively) and, more importantly, different net charges at the surface: at physiological pH 7.4, $GdNP_1$ had a slightly negative surface (zeta potential = −8 mV), whereas $GdNP_2$ had a definitely positive charge (+17 mV) (supplementary Figure S1). Hydrodynamic diameter is found in the range 3−5 nm for both GdNPs, with a polydispersity index of 35% (supplementary Figure S1).

Having a diameter of less than 10 nm, both GdNPs and IONPs penetrate into the cell interior. Labeling of endothelial cells with IONPs and stem cells with GdNPs yielded internalized masses (Fe or Gd, respectively) of between 1 and 10 pg per cell (Figure 2b). Electron microscopy, optical microscope, and confocal microscope observations localized both nanoparticles within

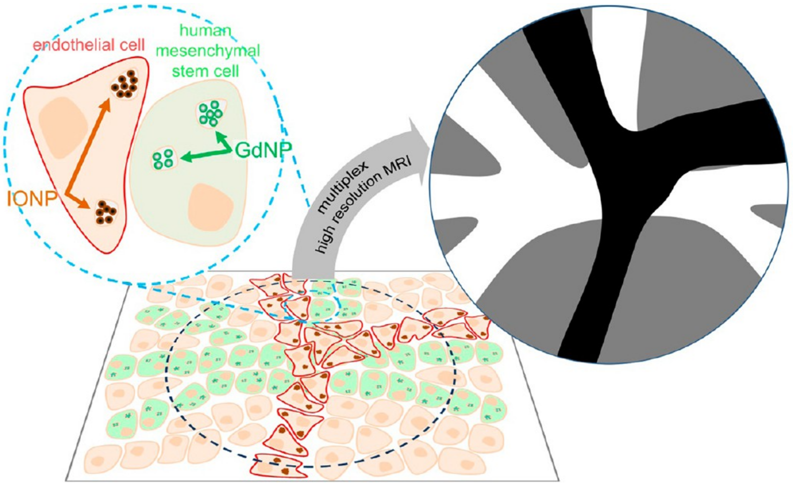

Figure 1. Cell-engineered tissue imaging: magnetic inorganic nanoparticles can be exploited in the deep analysis of engineered tissue. In particular, nanoparticles that differ in their magnetic behavior (*i.e.*, superparamagnetic and paramagnetic) could be used to identify different cell lineages by multiplex high-resolution MRI in multicellular constructs: the two cell types (*e.g.*, stem and endothelial cells) labeled with distinct gadolinium and iron oxide nanoparticles may remain visible, one in white and the other in black.

intracellular endosomal compartments (supplementary Figure S2). Thus, incubation for 1 h with IONP at [Fe] = 2.5 mM leads to the incorporation of 10 pg of Fe per endothelial cell, with no effect on cell functions (viability and proliferation; see supplementary Figure S3). Overnight incubation (12 h) is required for GdNP labeling, yielding 1 pg of Gd per stem cell after incubation with $GdNP_1$ at [Gd] = 5 mM and 2 and 10 pg of Gd after incubation with $GdNP_2$ at [Gd] = 1 mM and 5 mM, respectively. Note the more efficient incorporation of $GdNP_2$ compared to $GdNP_1$, attributed to the differences in their surface charges: the cellular negative membrane potentials likely promote the interaction between mesenchymal stem cells (MSCs) and $GdNP_2$ in comparison with negatively charged $GdNP_1$. Only the conditions corresponding to 10 pg of Gd per cell had a significant impact on cell viability (supplementary Figure S3). A comprehensive study of GdNP-labeled stem cell differentiation into bone (osteogenesis), fat (adipogenesis), and cartilage (chondrogenesis) was then conducted. For the three differentiation pathways and three intracellular amounts of Gd (1, 2, and 10 pg per MSC), no difference in the expression of differentiation-related genes (Figure 2c) or histological staining (Figure 2d) was found compared to control cells.

MRI Contrast Properties of Gd- and Fe-Labeled Cells. The longitudinal (r_1) and transverse (r_2) relaxivities of the two nanomaterials, both in solution and within cells, were then studied at different magnetic field strengths (Figure 3). In solution, IONPs exhibit the properties of T_2 agents ($r_2/r_1 > 10$, high r_2) and GdNPs the properties of T_1 agents ($r_1 \sim r_2$, high r_1). The NMRD profiles (changes in r_1 according to the applied magnetic field) always show a maximum at 0.1 T for IONPs and 1 T for GdNPs. At any field, the r_1 is superior for $GdNP_1$ in comparison with $GdNP_2$, in good agreement with the higher size of $GdNP_1$. At 4.7 T, the relaxation potential of both IONPs and GdNPs is thus favorable for negative and positive contrast, respectively: the r_1 of IONPs is greatly reduced, and the r_2/r_1 ratio therefore increases, while the r_1 of GdNPs is still high or increases.

Interestingly, the r_1 always decreased after the nanoparticles had been processed by the cells. With IONPs, the decrease following cell internalization was massive (100-fold or more), while r_2 fell only by a factor of 2.5. This resulted in a significant increase in the r_2/r_1 ratio, at 4.7 T, from 34 in solution to 330 intracellularly, thereby enhancing T_2-weighted cell detection. With GdNPs the r_1 fell far less, by a factor of 2.2 for $GdNP_1$ (1 pg of Gd per cell) and 2.6 and 3.8 for $GdNP_2$ (2 and 10 pg of Gd, respectively). Interestingly, r_2 did not decrease after cellular internalization; on the contrary, it rose by a factor of 1.1 in conditions of weak internalization (1 and 2 pg of Gd per cell) and 1.3-fold in conditions of stronger internalization (10 pg per cell). These changes led to a noteworthy increase in the r_2/r_1 ratio: at 4.7 T, r_2/r_1 rose from 2 in solution to respectively 4, 6, and 11 at 1, 2, and 10 pg of Gd per cell. Thus, intracellular confinement favored T_2-weighted detection of intracellular IONP but tended to undermine T_1-weighted detection of GdNP at high intracellular contents.

T_1 Imaging of Gd-Labeled Stem Cells at Cellular Resolution. To determine the T_1 imaging performance of Gd-labeled stem cells, they were seeded into porous polysaccharide biomaterials and were observed to distribute within the pores of the scaffold (see confocal microscopy images in Figure 4 and Figure S4 with zoomed observations of single cells, where stem cells exhibit green fluorescence, due to a membrane tag or to the FITC associated with $GdNP_1$). T_1-weighted and T_2-weighted images, described in detail in Materials

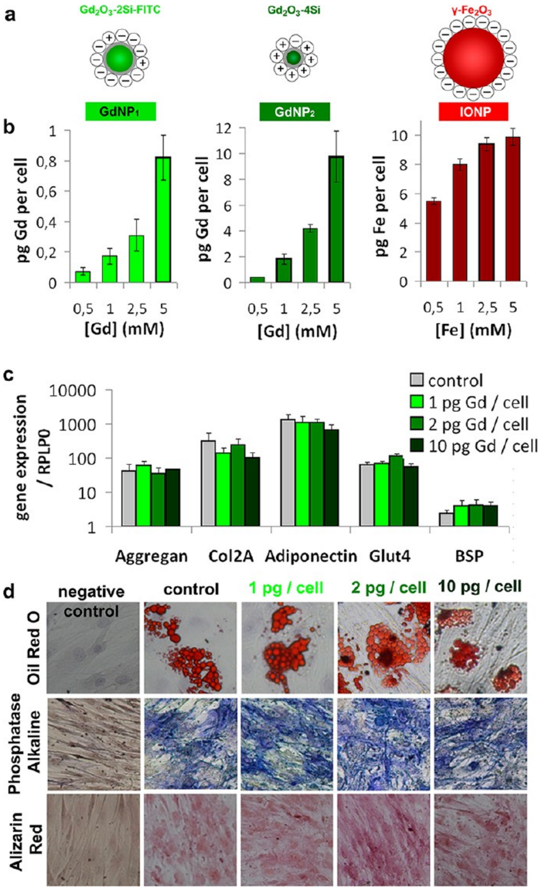

Figure 2. Gadolinium and iron oxide nanoparticles for cell labeling. (a) Gadolinium-based nanoparticles made of a polysiloxane network surrounded by covalently bound gadolinium chelates presenting a size of about 3 nm for $GdNP_1$ and 1.5 nm for $GdNP_2$. The iron oxide nanoparticles, 7 nm in diameter, are stabilized by citrate coating. (b) Incubation of mesenchymal stem cells (MSC) overnight with $GdNP_1$ and $GdNP_2$ leads to a cellular capture of between 0.1 and 1 pg of Gd per cell and 1 to 10 pg for $GdNP_1$ and $GdNP_2$, respectively. Conditions at 1 pg Gd/cell ($GdNP_1$); 2 and 10 pg Gd/cell ($GdNP_2$) were further analyzed. Incubation of endothelial cells with IONP for 1 h leads to 5 to 10 pg of iron internalized per cell. The condition at 10 pg/cell was selected. (c) MSC differentiation into chondrocytes, adipocytes, and osteocytes. Expressions of chondrogenic cartilage matrix genes aggregan and collagen II (col2A); of adipogenic specific genes Glut4 and AdipoQ; and of osteogenic bone sialoprotein (BSP) gene were measured by real-time PCR, normalized to RPLP0 mRNA and expressed in arbitrary units (means of three separate experiments ± SEM), with the negative control values taken as 1. No statistical difference using the Student's *t* test was observed between the different gadolinium labeling of the cells. (d) Adipogenic differentiation was also revealed for all conditions by accumulation of lipid vacuoles stained with oil red O. Osteogenesis was confirmed on histological sections by alkaline phosphatase activity (in blue) and calcium deposition (alizarin red). Similar adipogenic and osteogenic differentiations were obtained with nonlabeled and labeled cells, whatever the gadolinium concentration.

and Methods, were acquired on a 4.7 T MRI device equipped with a cryoprobe to image the biomaterials seeded with different numbers of cells (from 200 000 to 2 million). Images corresponding to a seeding with 2 million stem cells are shown in Figure 4, and with one and half million cells in supplementary Figure S5 and Figure S6, respectively. With 1 pg of Gd per cell ($GdNP_1$), the patterns of white spots observed on T_1-weighted images are remarkably similar to those obtained by confocal microscopy (Figure 4), whereas only the gel structure is visible on T_2-weighted images, resembling a control scaffold with no seeded cells (Figure S7). In this case the black spots on T_2-weighted images likely correspond to microbubbles that are not visible on T_1-weighted images. If the intracellular Gd content is increased to 2 pg of $GdNP_2$, the patterns of white spots resemble those obtained with 1 pg, but a black (cell) signal is now observed on T_2-weighted images, mostly co-localizing with the white pattern. As in these first two conditions, r_2 and r_1 are identical (see Figure 3); the difference is explained simply by the shortening of T_2 to half its value when the Gd content is increased by a factor 2.

Finally, at a higher intracellular Gd concentration (10 pg per cell), the cells appeared black on T_1-weighted sequences, and a strong black signal was detected on T_2-weighted sequences. At high levels of intracellular confinement, GdNPs therefore lose their ability to behave as a T_1 contrast agent, switching instead to T_2 contrast, in keeping with the increase in the r_2/r_1 ratio observed in these conditions. This highlights the role of intracellular confinement in the modulation of T_1 contrast properties. However, in the case of low Gd intracellular doses, the white cellular patterns observed are the first demonstration of the feasibility of Gd imaging at the cellular level.

The same imaging was performed with scaffolds seeded with endothelial cells labeled with IONPs (T_2 contrast agent). In this case the cells appeared black on both T_1 and T_2 sequences, with a total loss of signal on T_2 images for the 2 million cell condition shown in Figure 4, due to the excessive contrast of IONP-labeled cells. At lower cell numbers, IONP-labeled endothelial cells can be seen as individual black spots on T_2-weighted images (supplementary Figure S8), reaching a single-cell resolution, as previously reported in gels[32] or *in vivo*.[33,34] At this stage it must be noted that any improvement in T_1 relaxivity for the T_1 agents would be highly recommended to increase the sensitivity of cell detection. In contrast, given the large susceptibility artifact created by SPION-labeled cells, more efficient T_2 agents are not necessary since it could be detrimental to the resolution and prevent detailed imaging of cell pattern. Finally, we believe that in case both contrast agents are internalized in the same cell, only the r_2 effect dominates, preventing distinguishing double-labeled cells from single-IONP-labeled cells.

Dual Black and White Imaging *in Vitro* and *in Vivo*. Next, we examined the possibility of visualizing the two cell types simultaneously. Endothelial cells and stem cells were seeded in the same biomaterial, either on each side of the scaffold (symmetric seeding) or with

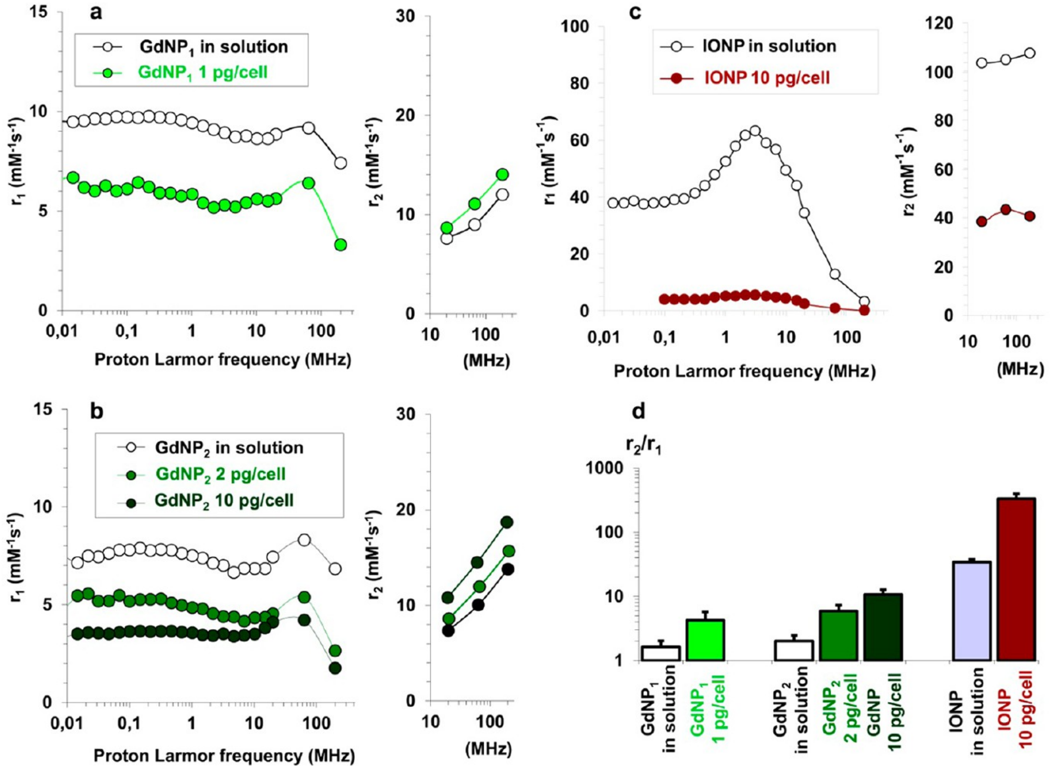

Figure 3. Nuclear magnetic relaxation dispersion (NMRD) r_1 and r_2 profiles for GdNP$_1$ (a), GdNP$_2$ (b), and IONP (c). For all NPs cell internalization induces a reduction of r_1 relaxivity as compared with that of the nanomaterials in solution. By contrast, GdNP cellular processing slightly increases the r_2 relaxivities while diminishing it for IONPs. (d) As a result, the ratio r_2/r_1 (signature of the T_2 *versus* T_1 imaging) gradually increases with the intracellular dose for GdNPs and dramatically increases for IONPs after cell internalization (note the use of a log scale).

endothelial cells in the center and stem cells at the periphery (spot seeding). Both seeding patterns gave rise to images (Figure 5 and Figure 6) with bright white cells on one side and black cells on the other side in the symmetric conditions, and endothelial cells appearing as black spots in the center surrounded by a white cloud of stem cells in the spot-seeding conditions. The cell localization within the scaffold was confirmed with confocal microscopy. By comparing the two imaging techniques, we found that the MRI resolution of detection of the different cell populations is close to 200 μm (supplementary Figure S9).

In Figure 6, this new dual MRI technique was tested *in vivo*. Biomaterials seeded with both cell types were implanted subcutaneously in mice flanks. On whole-mouse views, the scaffolds were perfectly identifiable, yielding a black and white signal (shown at day 1 in Figure 6 for spot-seeding pattern; other mice and seeding patterns are shown in supplementary Figure S10). High-resolution MRI provided the same resolution as the one obtained *in vitro*, and the cellular patterns closely matched those obtained by confocal microscopy prior to implantation. Of importance, the time duration to get a high-resolution T_1-weighted image was less than 10 min, making this *in vivo* imaging easily manageable. Moreover, the majority of the cells embedded within the transplanted scaffold were still viable at different times, as shown by hematoxylin and eosin staining (supplementary Figure S11). Even if the cell distribution evolved over time, with a more widespread MSC distribution on day 15 (Figure 6c), MRI did not provide quantitative information on the proliferation of the implanted stem cells.

Application to Vascular Tissue Engineering. Endothelial and stem cells were then combined within the same porous biomaterial, this time with a tubular shape (internal diameter less than 2 mm), in order to create a cellular graft with a structure mimicking that of a small-diameter blood vessel.[35] The main difficulty encountered with such small substitute vessels was attaching endothelial cells to the inner wall of the tube. Here we exploited IONPs not only as contrast tags but also as force mediators, by using an external magnet to force endothelial cells to form an endothelium (Figure 7). The tube was first seeded with a suspension of stem cells, which efficiently integrated the porous structure. Then, an endothelial cell suspension was introduced into the lumen, and the entire tube was placed inside a hollow cylindrical magnet. The endothelial cells were attracted efficiently to the inner walls (supplementary movie M2), leading to a rapid and uniform coverage. Confocal imaging unambiguously demonstrated the effectiveness of this approach by showing an endothelial layer lining the

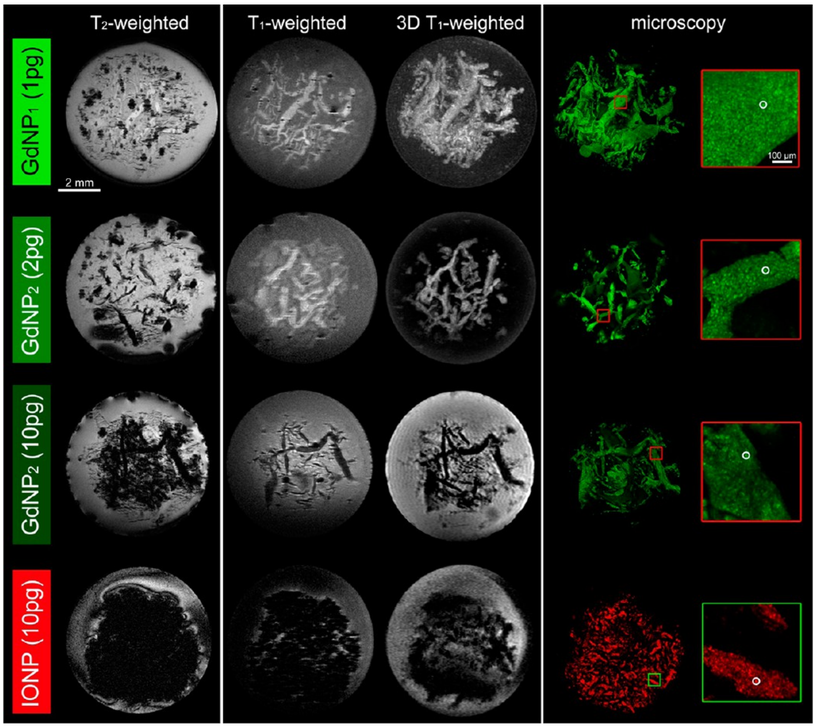

Figure 4. **MRI imaging of the polysaccharide biomaterials seeded with 2 million stem cells labeled with the three different doses of GdNPs or seeded with 2 million endothelial cells labeled with IONPs. T_2- and T_1-weighted sequences were acquired with the same acquisition parameters (described in the Materials and Methods section). A 3D T_1 sequence was also used to allow volume reconstruction. Prior to MRI, the same scaffolds were imaged by confocal microscopy at a 4× magnification. $GdNP_1$-MSCs were detected in green because of FITC molecules embedded in the silica shell, whereas $GdNP_2$-MSCs were counterstained at the membrane with PKH67 marker. Similarly, the HUVEC-C plasma membrane was stained in red by PKH26 marker. Single cells (circled in white as an example in the confocal imaging zoomed part on the right) appeared densely packed within the pores of the biomaterials.**

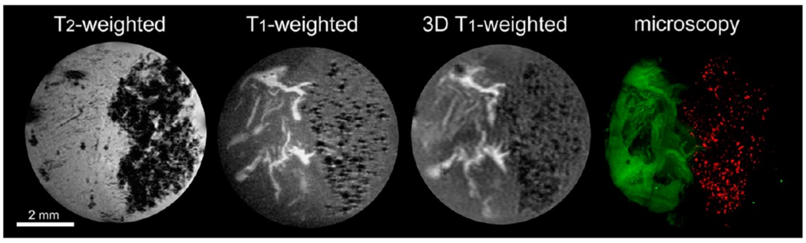

Figure 5. **Dual black and white imaging of stem cells and endothelial cells seeded in a biomaterial. On the right of the scaffold, the endothelial cells, labeled with IONPs, appear in black, with a strong contrast on T_2-weighted images, while on the left part, the stem cells, labeled with $GdNP_1$, appear in white on T_1-weighted images. Confocal microscopy confirmed the symmetric localization of the cells within the porous scaffolds (green, stem cells; red, endothelial cells).**

lumen and stem cells penetrating into the core of the substitute vessel. Histological observations also showed the cohesion of the magnetically formed endothelium and its attachment to the surface of the biomaterial (supplementary Figure S12). On high-resolution T_1-weighted MRI, the two cell layers were perfectly identifiable, with the endothelium in black and the muscle-generating stem cells in white (Figure 7, other views in supplementary Figure S13).

DISCUSSION

MRI contrast agents, either paramagnetic (gadolinium chelates) or superparamagnetic (iron oxide nanoparticles), have been developed for human diagnostic purposes. By creating local magnetic fields that modify the relaxation times of surrounding protons, they increase target sensitivity and precision. The use of such contrast agents to monitor cells is more recent, with the first pioneering studies in 2000,[36,37] and even more recently, the demonstration of MRI stem cell monitoring for therapy.[38,39] Cell labeling with iron oxide nanoparticles has since been extensively studied in order to ensure biological safety and innocuousness for cell functions.[40−43] In contrast, gadolinium has been used to label individual cells in only a few studies.[21−25,44,45] The inherent toxicity of free gadolinium has led to the development of gadolinium chelates as molecular contrast agents[46] or to label nano-objects.[47,48] For cell

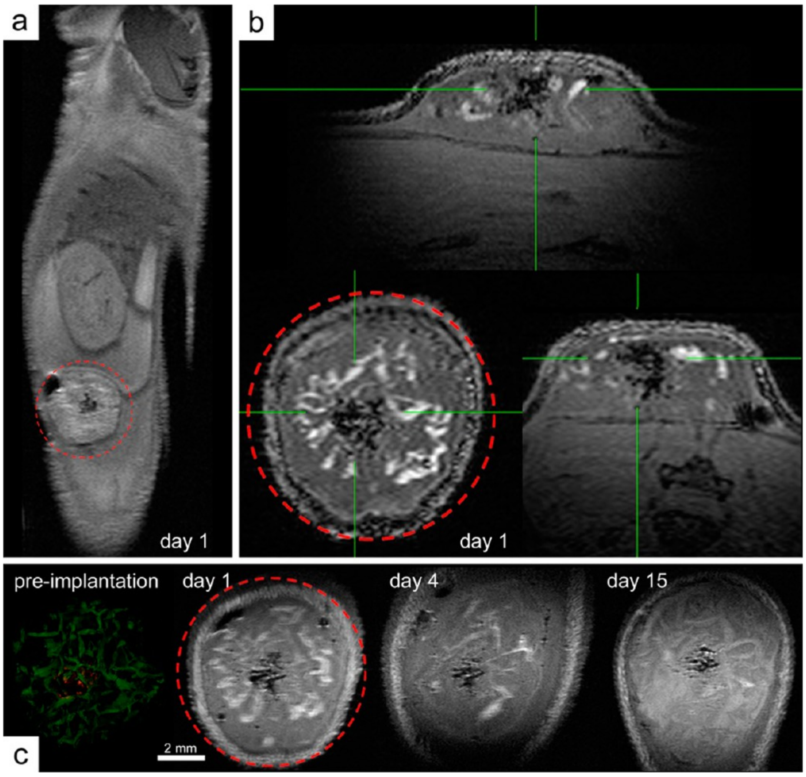

Figure 6. *In vivo* imaging of the dual spot seeding in scaffolds. (a) Right after implantation, at day 1, the scaffold was detected on whole-body images (voxel 150 μm), and the black and white contrast was already detected. (b) It was then further imaged at high resolution using the cryoprobe (voxel 49 μm). By 3D T_1-weighted analysis, orthogonal scans of the scaffold at day 1 are reported. A video of the 3D reconstruction (movie M1) is available as Supporting Information. (c) The evolution of the cellular patterns was monitored over time, up to day 15 (before implantation, left; the scaffold was imaged by confocal microscopy).

therapy applications, it is crucial that the labeling process does not affect the capacity for stem cell differentiation. Only three such studies have been performed with gadolinium, using Gd nanotubes,[49] mesoporous silica 100 nm particles,[50] or citrate-coated gadolinium oxide nanoparticles.[51] Here, we quantitatively investigated the dose-dependent uptake by mesenchymal stem cells of silica-coated gadolinium oxide nanoparticles with different surface charges and found no effect on cell viability for intracellular Gd load up to 10 pg. Moreover the stem cell capacity to differentiate into three different lineages (adipogenesis, osteogenesis, and chondrogenesis) was preserved. This finding further confirms the potential of a Gd-based nanoplatform as a nontoxic cellular tattoo for MRI cell tracking.

Remarkably the ability of Gd- and iron-based nanoplatforms to induce distinguishable positive and negative contrasts could be conserved once internalized by cells. It is well known that cellular compartmentalization into lysosomal structures drastically impacts longitudinal relaxivity, mainly due to the hampered accessibility of water protons to the confined T_1 or T_2 contrast agent.[52,53] This effect favors T_2 (and T_2*) detectability of labeled cells, by increasing the ratio r_2/r_1 in a dose-dependent manner. Here is the first observation of the effect of intracellular Gd confinement on the NMRD profile and first comparison of the effect of cellular processing on paramagnetic and superparamagnetic agents. While the NMRD profile of intracellular iron oxide is completely flattened, the profile of GdNPs is still peaked at high field following cell internalization. This suggests that the tumbling dynamics of GdNPs may not be affected by lysosome confinement, in contrast to iron oxide NPs, undergoing a drastic change in magnetic behavior upon cell internalization.[54] Thus the relative quenching effect of GdNPs probably results mostly from the slow exchange of water molecules across the cell and endosomal membranes. In consequence, for moderate internalization of GdNP (<10 pg), labeled cells could still be detected in white on T_1-weighted images, whereas cells tagged with iron oxide were black in any case.

In vivo, some transplanted labeled cells may die and release both Gd and Fe nanoparticles, potentially generating a confounding signal. Anyway, it is likely that these nanoparticles would remain entrapped in the scaffold pores and be recaptured by surrounding living cells, thus strongly limiting the risk of cellular signal loss. If, on the other hand, the released nanoparticles enter the bloodstream, they would be rapidly cleared by the reticuloendothelial system, ending up in the liver or spleen and again avoiding a false signal within the implant. However, if inflammatory cells are recruited

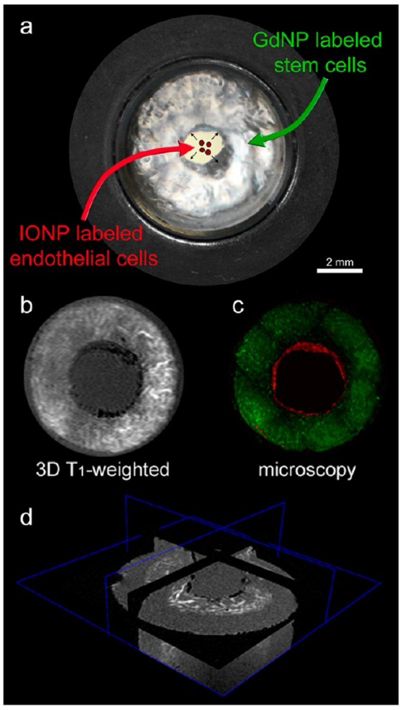

Figure 7. Development of small vascular substitutes monitored by MRI. Magnetic targeting was used to force the adhesion of the IONP-labeled endothelial cells on the lumen of a tubular-shaped scaffold. A video showing HUVEC-C (labeled with fluorescent PkH26 dye and IONP) attraction in the tube lumen is available as Supporting Information (movie M2). Stem cells were seeded directly into the tube bulk (a). The endothelial and stem cell layers were detected in black and white on T_1-weighted images, correlating perfectly the observation by confocal microscopy (b, c). A 3D reconstruction of a 3D T_1-weighted scan is reported, in which orthogonal slices focused on the correspondence of MSC and HUVEC-C seedings (d).

at the site of the implantation, they could as well process the released nanoparticles and dead cells, then leading to a confounding signal.

Such multicontrast labeling provides novel opportunities for noninvasive multicellular tracking. Indeed, in order to mimic the intercellular interactions that maintain tissue homeostasis, cell therapy could greatly benefit from heterotypic cell graft. Recent tissue-engineered approaches highlight the advantages of coculture for promoting tissue repair. For example, myocardial engineered tissues cultured with a network of endothelial cells can be more easily connected to host vessels, contributing to improve cardiac function.[55] Likewise, for cell therapy of a full-thickness burn, stem cells seeded in a biocompatible scaffold could be used to reconstruct the damaged area, while endothelial cells would be added to vascularize the graft and thus avoid necrosis.

As demonstrated here for the first time, a multilabeling technique would enable a personalized tracking of the different cell types involved in tissue regeneration. Regarding safety issues, the dose of the contrast agent (either iron oxide or GdNP) introduced in the body by the labeled cells is negligible in comparison to the intravenous dose administrated in current clinical practice. Nevertheless, the unique contrast properties of the iron- and Gd-based nanoplatform loaded in cells allow a differential monitoring of stem cell *versus* endothelial, together with anatomical details, in a single standard MRI acquisition. Nonconventional MRI contrast agents, such as chemical shift reagent (PARACEST agent)[56] and multinuclear reagent (^{19}F-containing label),[57,58] were recently proposed to detect specific cell populations. However these frequency-encoding techniques suffer from relatively low spatial resolution *in vivo* and rely on the use of nonclinical ^{19}F-MRI and MR spectroscopy. In addition, PARACEST agents are no more efficient when internalized in lysosomes and thus require electroporation for cell labeling.[56] In contrast, the method presented here uses a very standard MRI protocol, naturally occurring endocytosis of nanoplatforms without a transfection agent, and take advantage of the excellent resolution (50 μm) provided by a 4.7 T MRI scanner and dedicated cryoprobe to reveal multicellular organization at the cellular level in a tissue-engineered construct. Moreover we demonstrate MRI monitoring of the multicellular construct after *in vivo* implantation in a mouse model. Remarkably the imaging signature of the stem cells and endothelial cells, their specific spatial organization, and beginning of the supporting scaffold could still be identified in the host tissue over two weeks after implantation. Such MRI cell imaging has a crucial advantage over 3D optical microscopy, which is limited by the depth of observation. While nuclear imaging methods could also potentially use different isotopes to label two cell types, their resolution is far poorer than that of MRI, and their anatomical correlation is low. Therefore high-resolution multiplex MRI, which has no depth limitation, will provide a unique tool for monitoring the fate of therapeutic cells used to repair tissue damage. It will then be possible to monitor the reconstruction and healing process in depth, as well as the degradation of the supporting scaffold, its ability to deliver the therapeutic cells, the ability of these cells to integrate, proliferate, and vascularize the implant, and the time course of all these processes. Last but not least, superparamagnetic labeling of therapeutic cells affords the unique capability of magnetic manipulation, which can be exploited to mimic cellular organization of native tissue in engineered tissue constructs. Such magnetic control of endothelial cell localization, together with multicellular imaging, was successfully used here to engineer vessels.

The main limitation of the proposed method in the clinical setting would be similar to those encountered with the use of MRI for cell tracking, *i.e.*, nanoparticle dilution during cell division and leakage and intercellular transfer following cell death. Anyway, the first aim of the dual-cell tracking method is to monitor two cell types within an engineered tissue, in which stem cells may differentiate and stop proliferating, while nanoparticles released from dead cells would likely be trapped within the scaffold and immediately transferred to adjacent living cells. The inherent limitation of this dual method is then that only two codes can be detected, but further developments with complex MRI sequences could be envisaged to modulate the signal as a function of the intracellular amount of each contrast agent.

CONCLUSIONS

Here we demonstrated that therapeutic cells (endothelial cells and stem cells) labeled with distinct gadolinium and iron oxide nanomaterials can be visualized by high-resolution MRI. The two cell types remain visible, one in black and the other in white, when embedded in a biomaterial intended for tissue engineering and cell therapy. This method provides cellular-level resolution, deep within the body, along with the corresponding anatomical image. In addition, the use of magnetic nanoparticles provides new possibilities for cellular manipulation prior to implantation, by simple application of an external magnetic field. Here, by way of an example, we described the creation of a potential substitute vessel. In conclusion, the dual-label, black and white, high-resolution cellular MRI represents a major step toward the goal of noninvasive, *in vivo* monitoring of cell therapy products.

MATERIALS AND METHODS

Chemicals. MSCGM medium was purchased from Lonza. Dulbecco's modified Eagle medium (DMEM), fetal bovine serum (FBS), L-glutamine, penicillin−streptomycin, and phosphate-buffered saline (PBS) were obtained from Gibco. Paraformaldehyde, low-melting agarose, PKH26 red, and PKH67 green were purchased from Sigma-Aldrich. AlamarBlue was obtained from Life Technology. BD Matrigel Matrix was purchased from BD Bioscience.

Gadolinium Oxide and Iron Oxide Nanoparticles. The synthesis of the nanoparticles is a three-step process. The first step is the synthesis of a gadolinium oxide core followed by the growth of a polysiloxane shell in diethylene glycol (DEG). For $GdNP_1$, the gadolinium oxide cores were obtained by addition of an excess of soda on gadolinium trichloride at room temperature (core size of 3.5 nm). For $GdNP_2$, the synthesis of the cores is performed at high temperature (180 °C) with a lack of soda (core size of 1.5 nm). The second step is the growth of the polysiloxane shell on the gadolinium oxide core by addition of convenient quantities of silane precursors (APTES and TEOS) in appropriate ratios. The last step is the grafting of diethylenetriaminepentaacetic dianhydride in DEG before transfer to water. The addition of a sufficiently high amount of chelate led to the dissolution of the gadolinium oxide core and the complexation of the gadolinium by the chelates (final size of 3 nm for $GdNP_1$ and 1.5 nm for $GdNP_2$).[47] Beyond different sizes due to the synthesis protocols, the two GdNPs showed a difference in the variation of the net charge at the surface: indeed, by measuring the zeta potential as a function of pH, the $GdNP_1$ showed an inversion of net charge at pH 6.4, whereas a shift of the charge variation to pH 9.0 was observed for $GdNP_2$ (Figure S1).

Iron oxide nanoparticles were synthesized by alkaline coprecipitation of $FeCl_2$ (0.9 mol) and $FeCl_3$ (1.5 mol) salts, according to Massart's procedure. The IONPs used in this study had an average diameter of 7 nm (d_0 = 7 nm, polydispersity index $\sigma = 0.35$, volume fraction of nanoparticles in the suspension $\varphi = 3.1\%$, specific susceptibility χ/ϕ of 8.2). The volume fraction and average size of inorganic cores were determined by fitting the magnetization curve of IONPs using Langevin's law.

Zeta Potential Analysis. The zeta potential profiles of GdNP were analyzed by NanoZS (Malvern Instrument), equipped with a 4.0 mW He−Ne laser operating at 633 nm, an Avalanche photodiode detector, and an MPT-2 autotitrator. The zeta potential of GdNPs was determined by ranging the pH of the nanoparticle suspension from pH 12 to pH 4 (with steps of 0.5), by using 0.1 M solutions of NaOH and HCl. Each point corresponds to the average of 30 measurements.

Cell Labeling with Nanoparticles. Human mesenchymal stem cells were purchased from Lonza (#PT-2501). These adherent cells were cultured in MSCGM medium, in a humidified atmosphere at 37 °C and 5% CO_2. For gadolinium labeling, the stem cells were used at passages 4 to 8. Endothelial umbilical vein cells (HUVEC-C) were purchased from LGC Standards (#CRL-1730). The cells were cultured in DMEM medium supplemented with 10% FBS, L-glutamine (0.002 M), and penicillin/streptomycin (100 IU/mL) at 37 °C in a humidified atmosphere at 5% CO_2. For iron oxide labeling, the cells were used at passages below 40.

Concerning gadolinium labeling, nanoparticle powders ($GdNP_1$ or $GdNP_2$) were resuspended in supplemented MSCGM medium and gently mixed for 30 min, in order to obtain a stable suspension at 0.5, 1, 2.5, or 5 mM of gadolinium. Then, the culture medium was replaced with nanoparticle suspension, and confluent stem cells were incubated for 12 h. Confluent HUVEC cells were labeled by incubating cells with an IONP suspension (at 2.5 mM iron) for 60 min, followed by a chase period of 12 h in supplemented culture medium. The surface of the magnetic nanoparticles was stabilized with a coating of negatively charged citrate molecules.[30] The addition of free citrate in the culture medium prevents any aggregation of the nanoparticles, as previously established.[40]

$GdNP_2$-MSC and IONPs-HUVEC were fluorescently labeled respectively with PKH67 (green) and PKH26 (red) dyes (Sigma Aldrich).

Inductively Coupled Plasma Mass Spectrometry (ICP-MS) Analysis. Determination of gadolinium or iron content in labeled cells was performed by ICP-MS analysis (Agilent 7500ce). The samples were digested in concentrated HCl/HNO_3 (3:1, v/v) solution and diluted with ultrapure water for the analysis.

Stem Cell Differentiation, Staining, and RT-PCR. Labeled (with $GdNP_1$ and $GdNP_2$) and unlabeled stem cells were subjected to adipogenic, osteogenic, and chondrogenic differentiation to evaluate whether gadolinium labeling has any effect on their differentiation potential.

Adipogenic differentiation was performed in adipogenic medium consisting of DMEM high glucose containing 10% FBS, 100 U/mL penicillin, and 100 μg/mL streptomycin and supplemented with 100 μM insulin, 500 μM isobutylmethylanthine, 1 μM dexamethasone, and 200 μM indomethacin. Cells maintained in medium without any supplementation served as negative control. After 21 days of incubation in adipogenic medium, cells were fixed in 10% formalin, washed with deionized water and then with 2-propanol 60%, and stained for 10 min at room temperature in 0.3% oil red O (Sigma-Aldrich), rinsed with tap water, and then counterstained with hematoxylin (Sigma-Aldrich).

For osteogenic differentiation, 3×10^4 cells were seeded in six-well plates and grown for 21 days in DMEM low glucose containing 10% FBS, 100 U/mL penicillin, and 100 μg/mL streptomycin and supplemented with 0.1 μM dexamethasone, 50 μM L-ascorbic acid 2-phosphate, and 10 mM β-glycerophosphate (Sigma-Aldrich). Alkaline phosphatase was then histochemically stained by using a commercial kit (85L2, Sigma-Aldrich). Calcium mineralization was also determined using alizarin red S staining. Cells were fixed in 10% formalin, washed

TABLE 1. List of Primer Sequences for Gene Expression Analyses by Quantitative Real-Time PCR[a]

gene	accession number	sense primer	antisense primer
RPLP0	NM_053275.3	5′-TGCATCAGTACCCCATTCTATCA-3′	5′-AAGGTGTAATCCGTCTCCACAGA-3′
AGC	NM_001135.3	5′-TCTACCGCTGCGAGGTGAT-3′	5′-TGTAATGGAACACGATGCCTTT-3′
Col2A1	NM_001844.4	5′-ACTGGATTGACCCCAACCAA-3′	5′-TCCATGTTGCAGAAAACCTTCA-3′
BSP	NM_004967.3	5′-GGGCAGAGGAAATACTCAATCTGT-3′	5′-CAGTCCTGGAGTGAGGAAGCA-3′
Glut4	NM_001042.2	5′-GGACAGGAGACAAGAAATCCAGTT-3′	5′-GTCAACATGGACGCCGACTA-3′
AdipoQ	NM_004797.2	5′-GCAAAACCCATGGAGGAATTC-3′	5′-TCTTCCCTGACCCTGTTGGT-3′

[a] AGC: aggregane; Col2A1: collagen type II; BSP: bone sialoprotein; Glut4: soluble carrier family 2, member 4; AdipoQ: adiponectin.

with deionized water, stained 5 min at room temperature with 2% alizarin red S (Sigma-Aldrich), rinsed with tap water, and then counterstained with 1% light green (Sigma-Aldrich).

For chondrogenic differentiation, 2.5×10^5 cells were centrifuged (260 g) to induce a high-density pellet, which was cultured in serum-free DMEM high glucose containing 100 U/mL penicillin, 100 μg/mL streptomycin, 50 μM L-ascorbic acid 2-phosphate, 0.1 μM dexamethasone, 1 mM sodium pyruvate, 0.35 mM L-proline (Sigma-Aldrich), 1% ITS-Premix (BD Biosciences), and finally 10 ng/mL TGF-β3 (Interchim). Negative control was a pellet cultured in the same medium without TGF-β3.

At the end of all three differentiation protocols, total RNAs were prepared using the total RNA isolation kit (Machery-Nagel). Complementary DNA was synthesized using SuperScript II Reverse Transcriptase (Life Technologies), from 1 μg of total RNA in a final volume of 100 μL. Real-time quantitative RT-PCR for five genes (Table 1) was performed in duplicate with the ABI PRISM 7900 sequence detection system and SYBRGreen dye (Applied Biosystems, Foster City, CA, USA). The fluorescence cycle threshold was calculated to quantify the relative amount of gene expression. The mRNA levels of genes of interest were expressed relative to levels of RPLP0. Student's *t* test for paired data was used to statistically analyze differences between the different labeling conditions.

Cell Seeding in Biomaterials. Polysaccharide-based scaffolds were prepared using a mixture of pullulan/dextran (75:25) with the cross-linking agent sodium trimetaphosphate at 11% (w/v) under alkaline conditions.[59] Pores were created by a gas foaming technique using sodium carbonate in 20% acetic acid solution.[60] Scaffolds were freeze-dried for 48 h for complete removal of water and stored at room temperature until use. Prior to cell seeding, the scaffolds were punched into discs having a cylindrical shape of 8 mm in diameter and 3 mm in thickness.

For the seeding in porous scaffolds, cells were trypsinized, counted, and resuspended at the desired concentration ($(0.5-2) \times 10^6$ cells) in 40 μL of culture medium. The suspension was slowly added to the dry scaffold, by covering the entire surface. After hydratation, scaffolds became transparent and maintained a regular internal lamellar pore structure, with porosity of about 200 μm.

For the dual-seeded scaffold, 2×10^5 IONPs-HUVEC-C were resuspended in 15 μL of culture medium and used to hydrate a half scaffold. After 2 min, the opposite scaffold side was hydrated with 20 μL of a suspension containing 2×10^6 GdNPs-MSCs. For the spot scaffold, 2×10^4 IONPs-HUVEC-C were resuspended in 2.5 μL of medium and seeded at the center of the scaffold. After 2 min, the entire scaffold was hydrated with 40 μL of GdNPs-MSC (2×10^6 cells). All the hydrated scaffolds were placed at 37 °C for 5 min in order to properly pack the cells in the pores; then culture medium was added to the culture dish in order to completely cover the seeded scaffold. Scaffolds were cultured for 36 h, washed twice with PBS (5 min per step), and fixed in 4% paraformaldehyde for 30 min at 4 °C. Fixed scaffolds were washed twice with PBS, analyzed by confocal microscopy, and then embedded in a 0.3% low-melting agarose gel for MRI characterization.

Toward the Fabrication of a Substitute Vessel. A tubular-shaped polysaccharide scaffold was used to simulate the vessel geometry. The nonhydrated tube had an external diameter of 6 mm, a lumen diameter of 2 mm, and a length of 8 mm. The scaffold was first seeded with a suspension of GdNPs-MSC (2×10^6 in 50 μL), by hydrating the tube's outer surface. The tube was then inserted into a sterile hollow cylinder permanent magnet. The magnetic force experienced by the cells when inserted inside the lumen was calibrated by tracking cell migration (see supplementary movie M2) in concentric circles with an increment of 150 μm and balancing the measured viscous force ($6\pi \times$ viscosity $\times$ cell radius $\times$ cell velocity) by the magnetic one. The magnetic forces applied to the cells at the tube luminal surface were found in the 2 pN range.

A protein coating of the lumen was achieved by filling the cavity with cold BD Matrigel Matrix (BD Bioscience, #356234, 25 μL) for 30 s. After removing the excess of protein matrix, 20 μL of IONPs-HUVEC-C suspension (4×10^4 cells) was seeded in the lumen. After 4 h, the magnet was removed and the tube was cultured for 36 h before fixation in 4% paraformaldehyde.

Microscope Imaging of the Cellularized Constructs. Confocal microscope images were acquired by using an Andor Technology with Olympus JX81/BX61 device/Yokogawa CSU device spinning disk microscope (Andor Technology plc, Belfast, Northern Ireland), equipped with a 60× Plan-ApoN oil objective lens (60×/1.42 oil, Olympus) or 4× UPlan-FI objective lens (4×/0.13, Olympus). Samples were excited at 488 nm for detection of GdNP$_1$-MSC and GdNP$_2$-MSC (λ_{em} = 525 ± 15 nm) and at 561 nm for IONPs-HUVEC-C (λ_{em} = 608 ± 18 nm). Image acquisitions and 3D reconstruction were obtained by Andor iQ2 software and postprocessed with ImageJ opensource software.

Implantation in Mice. Animals were handled according to the European Community guidelines for the care and use of laboratory animals (European Directive 86/609/EEC on the protection of animals used for experimental and other scientific purposes and its amendment (2003/65/EC)). The Institutional Animal Care and Use Committee of Paris Cardiovascular Research Center (PARCC) approved animal protocols. Six-week-old NMRI nude mice (weighing 32 ± 1 g, provided by Janvier, France) were housed in polypropylene cages and were provided with food and water *ad libitum*. For scaffold implantation, six mice were anesthetized with ketamine/xylazine intraperitonally (10 and 50 mg/kg, respectively). Seeded scaffolds (diameter of 6 mm) were implanted subcutaneously on a flank, and the skin was closed with 4/0 sutures (Ethicon). At days 1, 4, 8, and 15, mice were anesthetized by administration of isoflurane in air (supplied at a flow rate of 1 L/min) and imaged by MRI (at least three animals were analyzed at each time point). The induction of anesthesia was obtained with a mixture of isoflurane at 3%, whereas a mixture at 0.5% was used for its maintenance. At the end of the experimental protocol, mice were sacrificed with a lethal injection of sodium pentobarbital.

MRI Imaging. Magnetic resonance imaging was performed on a BrukerBio-Spec 47/40 USR scanner or a 40 cm bore actively shielded 4.7 T scanner equipped with a cryogenic surface coil (CryoProbe) or a whole-volume radiofrequency (RF) coil, in the Small Animal Imaging Platform Paris-Descartes (PARCC-HEGP). The scanner was interfaced to ParaVision software for preclinical MRI research. All fixed scaffolds were imaged with the cryogenic probe by (i) 2D fast spin echo sequence (referred to as T_1-weighted) with a TE of 12 ms and a TR of 190, 442, or 2000 ms, flip angle of 180°, in-plane resolution of 39 μm, 20 averages, slice thickness of 200 nm for a total of seven slices; (ii) 3D gradient echo sequence (ran under fast imaging with steady-state precession

TABLE 2. [a]

sequence	probe	TR (ms)	TE (ms)	flip angle	resolution (μm)	average	acq time
				Scaffold Imaging			
fast spin echo	CP	190	12	180°	39	20	3 min 2 s
	CP	442	12	180°	39	20	7 min 4 s
	CP	2000	12	180°	39	20	16 min
3D-GE	CP	16	3	25°	$50 \times 50 \times 50$	2	17 min 8 s
T_2-weighted	CP	750	20	50°	39	4	8 min 39 s
				Animal Imaging			
fast spin echo	CP	442	12	180°	39	30	8 min
	VC	442	12	180°	150	30	15 min
3D-GE	CP	16	3	25°	$83 \times 83 \times 83$	2	10 min 17 s

[a] Abbreviations: TR = repetition time, TE = echo time, 3D-GE = three-dimensional gradient echo, CP = CryoProbe, VC = whole-volume RF coil.

protocol on free induction decay mode, referred to as 3D T_1-weighted), with a TE of 3 ms and a TR of 16 ms, flip angle of 25°, resolution of $50 \times 50 \times 50\ \mu m^3$, two averages; and (iii) 2D T_2-weighted fast low angle shot sequence with a TE of 20 ms and a TR of 750 ms, flip angle of 50°, in-plane resolution of 39 μm, four averages, slice thickness of 285 nm for a total of 11 slices. After surgery animals underwent whole-body MRI and a localized high-resolution MRI of the implant according to the following imaging protocols: (i) fast spin echo sequence with a TE of 12 ms and a TR of 442 ms, flip angle of 180°, 30 averages, in-plane resolution of 150 μm obtained with the volume RF coil or 39 μm with the cryogenic probe, slice thickness of 500 nm with the volume RF coil or 200 nm with the cryogenic probe, for a total of seven slices for both probes; (ii) 3D gradient echo sequence with a TE of 3 ms and a TR of 16 ms, flip angle of 25°, resolution of $83 \times 83 \times 83\ \mu m^3$ (cryogenic probe), two averages. (See Table 2.)

***Ex Vivo* Histological Imaging.** Scaffolds were retrieved from the mice after sacrifice. They were then fixed in 10% buffered formalin before being embedded in optimal cutting temperature (OCT) compound and frozen in a 2-propanol bath, cooled with liquid nitrogen. Cryosections (16 μm) were first observed by confocal microscopy to detect retained fluorescent signal from grafted cells.

Conflict of Interest: The authors declare no competing financial interest.

Supporting Information Available: Synthetic GdNP procedure and complementary details on cell labeling (Figures S1 to S3) and imaging in biomaterials *in vitro* and *in vivo* (Figures S4 to S13) are available free of charge *via* the Internet at http://pubs.acs.org.

Acknowledgment. The authors thank G. Autret, S. Kusmia, J. Kolosnjaj-Tabi, and O. Clément for MRI experiments and image processing; C. Péchoux and S. Chat for electron transmission microscopy; and P. Mowat for ICP-MS characterization. This work was supported by the French Research Funding Agency (ANR) within the framework of the MagStem Project (ANR-11 SVSE5) and NMVASC (ANR-10 INTB-1502-01), and by the European Project Magnifyco (Contract NMP4-SL-2009-228622).

REFERENCES AND NOTES

1. Place, E. S.; Evans, N. D.; Stevens, M. M. Complexity in Biomaterials for Tissue Engineering. *Nat. Mater.* **2009**, *8*, 457–470.
2. Atala, A.; Kasper, F. K.; Mikos, A. G. Engineering Complex Tissues. *Sci. Transl. Med.* **2012**, *4*, 160rv12.
3. Gauvin, R.; Khademhosseini, A. Microscale Technologies and Modular Approaches for Tissue Engineering: Moving toward the Fabrication of Complex Functional Structures. *ACS Nano* **2011**, *5*, 4258–4264.
4. Heeger, C. H.; Jaquet, K.; Thiele, H.; Zulkarnaen, Y.; Cuneo, A.; Haller, D.; Kivelitz, D.; Schmidt, T.; Krause, K.; Metzner, A.; *et al.* Percutaneous, Transendocardial Injection of Bone Marrow-Derived Mononuclear Cells in Heart Failure Patients Following Acute St-Elevation Myocardial Infarction: Alster-Stem Cell Trial. *EuroIntervention* **2012**, *8*, 732–742.
5. Mahou, P.; Zimmerley, M.; Loulier, K.; Matho, K. S.; Labroille, G.; Morin, X.; Supatto, W.; Livet, J.; Debarre, D.; Beaurepaire, E. Multicolor Two-Photon Tissue Imaging by Wavelength Mixing. *Nat. Methods* **2012**, *9*, 815–818.
6. Dong, N. N.; Pedroni, M.; Piccinelli, F.; Conti, G.; Sbarbati, A.; Ramirez-Hernandez, J. E.; Maestro, L. M.; Iglesias-de la Cruz, M. C.; Sanz-Rodriguez, F.; Juarranz, A.; *et al.* NIR-to-NIR Two-Photon Excited CaF_2:Tm^{3+},Yb^{3+} Nanoparticles: Multifunctional Nanoprobes for Highly Penetrating Fluorescence Bio-Imaging. *ACS Nano* **2011**, *5*, 8665–8671.
7. Norris, F. C.; Betts-Henderson, J.; Wells, J. A.; Cleary, J. O.; Siow, B. M.; Walker-Samuel, S.; McCue, K.; Salomoni, P.; Scambler, P. J.; Lythgoe, M. F. Enhanced Tissue Differentiation in the Developing Mouse Brain Using Magnetic Resonance Micro-Histology. *Magn. Reson. Med.* **2012**, in press, DOI: 10.1002/mrm.24573.
8. Sandiford, L.; Phinikaridou, A.; Protti, A.; Meszaros, L. K.; Cui, X.; Yan, Y.; Frodsham, G.; Williamson, P. A.; Gaddum, N.; Botnar, R. M.; *et al.* Bisphosphonate-Anchored Pegylation and Radiolabeling of Superparamagnetic Iron Oxide: Long-Circulating Nanoparticles for *in Vivo* Multimodal (T1MRI-Spect) Imaging. *ACS Nano* **2013**, *7*, 500–512.
9. Wang, H. H.; Lin, C. A.; Lee, C. H.; Lin, Y. C.; Tseng, Y. M.; Hsieh, C. L.; Chen, C. H.; Tsai, C. H.; Hsieh, C. T.; Shen, J. L.; *et al.* Fluorescent Gold Nanoclusters as a Biocompatible Marker for *in Vitro* and *in Vivo* Tracking of Endothelial Cells. *ACS Nano* **2011**, *5*, 4337–4344.
10. Chen, G.; Shen, J.; Ohulchanskyy, T. Y.; Patel, N. J.; Kutikov, A.; Li, Z.; Song, J.; Pandey, R. K.; Agren, H.; Prasad, P. N.; *et al.* (Alpha-$NaYbF_4$:Tm(3+))/CaF_2 Core/Shell Nanoparticles with Efficient near-Infrared to near-Infrared Upconversion for High-Contrast Deep Tissue Bioimaging. *ACS Nano* **2012**, *6*, 8280–8287.
11. Chung, H. J.; Lee, H.; Bae, K. H.; Lee, Y.; Park, J.; Cho, S. W.; Hwang, J. Y.; Park, H.; Langer, R.; Anderson, D.; *et al.* Facile Synthetic Route for Surface-Functionalized Magnetic Nanoparticles: Cell Labeling and Magnetic Resonance Imaging Studies. *ACS Nano* **2011**, *5*, 4329–4336.
12. Bennewitz, M. F.; Lobo, T. L.; Nkansah, M. K.; Ulas, G.; Brudvig, G. W.; Shapiro, E. M. Biocompatible and pH-Sensitive PLGA Encapsulated MnO Nanocrystals for Molecular and Cellular MRI. *ACS Nano* **2011**, *5*, 3438–3446.
13. Modo, M.; Hoehn, M.; Bulte, J. W. Cellular MR Imaging. *Mol. Imaging* **2005**, *4*, 143–164.
14. Terrovitis, J. V.; Bulte, J. W.; Sarvananthan, S.; Crowe, L. A.; Sarathchandra, P.; Batten, P.; Sachlos, E.; Chester, A. H.; Czernuszka, J. T.; Firmin, D. N.; *et al.* Magnetic Resonance Imaging of Ferumoxide-Labeled Mesenchymal Stem Cells Seeded on Collagen Scaffolds-Relevance to Tissue Engineering. *Tissue Eng.* **2006**, *12*, 2765–2775.
15. Ramaswamy, S.; Greco, J. B.; Uluer, M. C.; Zhang, Z.; Fishbein, K. W.; Spencer, R. G. Magnetic Resonance Imaging of Chondrocytes Labeled with Superparamagnetic Iron Oxide Nanoparticles in Tissue-Engineered Cartilage. *Tissue Eng. Part A* **2009**, *15*, 3899–3910.
16. Poirier-Quinot, M.; Frasca, G.; Wilhelm, C.; Luciani, N.; Ginefri, J. C.; Darrasse, L.; Letourneur, D.; Le Visage, C.; Gazeau, F. High-Resolution 1.5-T Magnetic Resonance Imaging for Tissue-Engineered Constructs: A Noninvasive Tool to Assess Three-Dimensional Scaffold Architecture and Cell Seeding. *Tissue Eng. Part C: Methods* **2010**, *16*, 185–200.
17. Harrington, J. K.; Chahboune, H.; Criscione, J. M.; Li, A. Y.; Hibino, N.; Yi, T.; Villalona, G. A.; Kobsa, S.; Meijas, D.; Duncan, D. R.; *et al.* Determining the Fate of Seeded Cells in Venous Tissue-Engineered Vascular Grafts Using Serial MRI. *Faseb J.* **2011**, *25*, 4150–4161.
18. Liu, J. S.; Gartner, Z. J. Directing the Assembly of Spatially Organized Multicomponent Tissues from the Bottom Up. *Trends Cell Biol.* **2012**, *22*, 683–691.
19. Fayol, D.; Frasca, G.; Le Visage, C.; Gazeau, F.; Luciani, N.; Wilhelm, C. Use of Magnetic Forces to Promote Stem Cell

Aggregation during Differentiation, and Cartilage Tissue Modeling. *Adv. Mater.* **2013**, *25*, 2611–2616.

20. Caravan, P. Strategies for Increasing the Sensitivity of Gadolinium Based MRI Contrast Agents. *Chem. Soc. Rev.* **2006**, *35*, 512–523.
21. Geninatti-Crich, S.; Szabo, I.; Alberti, D.; Longo, D.; Aime, S. MRI of Cells and Mice at 1 and 7 T with Gd-Targeting Agents: When the Low Field Is Better!. *Contrast Media Mol. Imaging* **2011**, *6*, 421–425.
22. Faucher, L.; Tremblay, M.; Lagueux, J.; Gossuin, Y.; Fortin, M. A. Rapid Synthesis of PEGylated Ultrasmall Gadolinium Oxide Nanoparticles for Cell Labeling and Tracking with MRI. *ACS Appl. Mater. Interfaces* **2012**, *4*, 4506–4515.
23. Klasson, A.; Ahren, M.; Hellqvist, E.; Soderlind, F.; Rosen, A.; Kall, P. O.; Uvdal, K.; Engstrom, M. Positive MRI Contrast Enhancement in THP-1 Cells with Gd_2O_3 Nanoparticles. *Contrast Media Mol. Imaging* **2008**, *3*, 106–111.
24. Vuu, K.; Xie, J.; McDonald, M. A.; Bernardo, M.; Hunter, F.; Zhang, Y.; Li, K.; Bednarski, M.; Guccione, S. Gadolinium-Rhodamine Nanoparticles for Cell Labeling and Tracking *via* Magnetic Resonance and Optical Imaging. *Bioconjugate Chem.* **2005**, *16*, 995–999.
25. Ribot, E. J.; Miraux, S.; Delville, M. H.; Bouchaud, V.; Lacomme, S.; Gontier, E.; Bouzier-Sore, A. K.; Franconi, J. M.; Thiaudiere, E.; Voisin, P. Study of the MR Relaxation of Microglia Cells Labeled with Gd-DTPA-Bearing Nanoparticles. *Contrast Media Mol. Imaging* **2009**, *4*, 109–117.
26. Loai, Y.; Ganesh, T.; Cheng, H. L. Concurrent Dual Contrast for Cellular Magnetic Resonance Imaging Using Gadolinium Oxide and Iron Oxide Nanoparticles. *Int. J. Mol. Imaging* **2012**, *2012*, 230942.
27. Rima, W.; Sancey, L.; Aloy, M. T.; Armandy, E.; Alcantara, G. B.; Epicier, T.; Malchere, A.; Joly-Pottuz, L.; Mowat, P.; Lux, F.; *et al*. Internalization Pathways into Cancer Cells of Gadolinium-Based Radiosensitizing Nanoparticles. *Biomaterials* **2013**, *34*, 181–195.
28. Pirraco, R. P.; Melo-Ferreira, B.; Santos, T. C.; Frias, A. M.; Marques, A. P.; Reis, R. L. Adipose Stem Cell-Derived Osteoblasts Sustain the Functionality of Endothelial Progenitors from the Mononuclear Fraction of Umbilical Cord Blood. *Acta Biomater.* **2013**, *9*, 5234–5242.
29. Xu, T.; Zhao, W.; Zhu, J. M.; Albanna, M. Z.; Yoo, J. J.; Atala, A. Complex Heterogeneous Tissue Constructs Containing Multiple Cell Types Prepared by Inkjet Printing Technology. *Biomaterials* **2013**, *34*, 130–139.
30. Wilhelm, C.; Gazeau, F. Universal Cell Labelling with Anionic Magnetic Nanoparticles. *Biomaterials* **2008**, *29*, 3161–3174.
31. Le Duc, G.; Miladi, I.; Alric, C.; Mowat, P.; Brauer-Krisch, E.; Bouchet, A.; Khalil, E.; Billotey, C.; Janier, M.; Lux, F.; *et al.* Toward an Image-Guided Microbeam Radiation Therapy Using Gadolinium-Based Nanoparticles. *ACS Nano* **2011**, *5*, 9566–9574.
32. Smirnov, P.; Gazeau, F.; Beloeil, J. C.; Doan, B. T.; Wilhelm, C.; Gillet, B. Single-Cell Detection by Gradient Echo 9.4 T MRI: A Parametric Study. *Contrast Media Mol. Imaging* **2006**, *1*, 165–174.
33. Smirnov, P.; Poirier-Quinot, M.; Wilhelm, C.; Lavergne, E.; Ginefri, J. C.; Combadiere, B.; Clement, O.; Darrasse, L.; Gazeau, F. *In Vivo* Single Cell Detection of Tumor-Infiltrating Lymphocytes with a Clinical 1.5 T MRI System. *Magn. Reson. Med.* **2008**, *60*, 1292–1297.
34. Al Faraj, A.; Luciani, N.; Kolosnjaj-Tabi, J.; Mattar, E.; Clement, O.; Wilhelm, C.; Gazeau, F. Real-Time High-Resolution Magnetic Resonance Tracking of Macrophage Subpopulations in a Murine Inflammation Model: A Pilot Study with a Commercially Available Cryogenic Probe. *Contrast Media Mol. Imaging* **2013**, *8*, 193–203.
35. Fayol, D.; Visage, C. L.; Ino, J.; Gazeau, F.; Letourneur, D.; Wilhelm, C. Design of Biomimetic Vascular Grafts with Magnetic Endothelial Patterning. *Cell Transplant* **2013**, in press, DOI: 10.3727/096368912X6661300.
36. Bulte, J. W.; Douglas, T.; Witwer, B.; Zhang, S. C.; Strable, E.; Lewis, B. K.; Zywicke, H.; Miller, B.; van Gelderen, P.; Moskowitz, B. M.; *et al.* Magnetodendrimers Allow Endosomal Magnetic Labeling and *in Vivo* Tracking of Stem Cells. *Nat. Biotechnol.* **2001**, *19*, 1141–1147.
37. Lewin, M.; Carlesso, N.; Tung, C. H.; Tang, X. W.; Cory, D.; Scadden, D. T.; Weissleder, R. Tat Peptide-Derivatized Magnetic Nanoparticles Allow *in Vivo* Tracking and Recovery of Progenitor Cells. *Nat. Biotechnol.* **2000**, *18*, 410–414.
38. Nohroudi, K.; Arnhold, S.; Berhorn, T.; Addicks, K.; Hoehn, M.; Himmelreich, U. *In Vivo* MRI Stem Cell Tracking Requires Balancing of Detection Limit and Cell Viability. *Cell Transplant* **2010**, *19*, 431–441.
39. Ramos-Cabrer, P.; Justicia, C.; Wiedermann, D.; Hoehn, M. Stem Cell Mediation of Functional Recovery after Stroke in the Rat. *PLoS One* **2010**, *5*, e12779.
40. Fayol, D.; Luciani, N.; Lartigue, L.; Gazeau, F.; Wilhelm, C. Managing Magnetic Nanoparticle Aggregation and Cellular Uptake: A Precondition for Efficient Stem-Cell Differentiation and MRI Tracking. *Adv. Healthcare Mater.* **2013**, *2*, 313–325.
41. Soenen, S. J.; Hodenius, M.; De Cuyper, M. Magnetoliposomes: Versatile Innovative Nanocolloids for Use in Biotechnology and Biomedicine. *Nanomedicine (London)* **2009**, *4*, 177–191.
42. Long, C. M.; Bulte, J. W. *In Vivo* Tracking of Cellular Therapeutics Using Magnetic Resonance Imaging. *Expert Opin. Biol. Ther.* **2009**, *9*, 293–306.
43. Nejadnik, H.; Henning, T. D.; Castaneda, R. T.; Boddington, S.; Taubert, S.; Jha, P.; Tavri, S.; Golovko, D.; Ackerman, L.; Meier, R.; *et al*. Somatic Differentiation and MR Imaging of Magnetically Labeled Human Embryonic Stem Cells. *Cell Transplant* **2012**, *21*, 2555–2567.
44. Tseng, C. L.; Shih, I. L.; Stobinski, L.; Lin, F. H. Gadolinium Hexanedione Nanoparticles for Stem Cell Labeling and Tracking *via* Magnetic Resonance Imaging. *Biomaterials* **2010**, *31*, 5427–5435.
45. Figueiredo, S.; Cutrin, J. C.; Rizzitelli, S.; De Luca, E.; Moreira, J. N.; Geraldes, C. F.; Aime, S.; Terreno, E. MRI Tracking of Macrophages Labeled with Glucan Particles Entrapping a Water Insoluble Paramagnetic Gd-Based Agent. *Mol. Imaging Biol.* **2013**, *15*, 307–315.
46. Laurent, S.; Elst, L. V.; Muller, R. N. Comparative Study of the Physicochemical Properties of Six Clinical Low Molecular Weight Gadolinium Contrast Agents. *Contrast Media Mol. Imaging* **2006**, *1*, 128–137.
47. Lux, F.; Mignot, A.; Mowat, P.; Louis, C.; Dufort, S.; Bernhard, C.; Denat, F.; Boschetti, F.; Brunet, C.; Antoine, R.; *et al.* Ultrasmall Rigid Particles as Multimodal Probes for Medical Applications. *Angew. Chem., Int. Ed.* **2011**, *50*, 12299–12303.
48. Santra, S.; Jativa, S. D.; Kaittanis, C.; Normand, G.; Grimm, J.; Perez, J. M. Gadolinium-Encapsulating Iron Oxide Nanoprobe as Activatable NMR/MRI Contrast Agent. *ACS Nano* **2012**, *6*, 7281–7294.
49. Tran, L. A.; Krishnamurthy, R.; Muthupillai, R.; Cabreira-Hansen Mda, G.; Willerson, J. T.; Perin, E. C.; Wilson, L. J. Gadonanotubes as Magnetic Nanolabels for Stem Cell Detection. *Biomaterials* **2010**, *31*, 9482–9491.
50. Hsiao, J. K.; Tsai, C. P.; Chung, T. H.; Hung, Y.; Yao, M.; Liu, H. M.; Mou, C. Y.; Yang, C. S.; Chen, Y. C.; Huang, D. M. Mesoporous Silica Nanoparticles as a Delivery System of Gadolinium for Effective Human Stem Cell Tracking. *Small* **2008**, *4*, 1445–1452.
51. Shi, Z.; Neoh, K. G.; Kang, E. T.; Shuter, B.; Wang, S. C. Bifunctional Eu(3+)-Doped Gd(2)O(3) Nanoparticles as a Luminescent and T(1) Contrast Agent for Stem Cell Labeling. *Contrast Media Mol. Imaging* **2010**, *5*, 105–111.
52. Terreno, E.; Geninatti Crich, S.; Belfiore, S.; Biancone, L.; Cabella, C.; Esposito, G.; Manazza, A. D.; Aime, S. Effect of the Intracellular Localization of a Gd-Based Imaging Probe on the Relaxation Enhancement of Water Protons. *Magn. Reson. Med.* **2006**, *55*, 491–497.
53. Strijkers, G. J.; Hak, S.; Kok, M. B.; Springer, C. S., Jr.; Nicolay, K. Three-Compartment T1 Relaxation Model for Intracellular Paramagnetic Contrast Agents. *Magn. Reson. Med.* **2009**, *61*, 1049–1058.

54. Levy, M.; Wilhelm, C.; Devaud, M.; Levitz, P.; Gazeau, F. How Cellular Processing of Superparamagnetic Nanoparticles Affects Their Magnetic Behavior and NMR Relaxivity. *Contrast Media Mol. Imaging* **2012**, *7*, 373–383.
55. Sekine, H.; Shimizu, T.; Hobo, K.; Sekiya, S.; Yang, J.; Yamato, M.; Kurosawa, H.; Kobayashi, E.; Okano, T. Endothelial Cell Coculture within Tissue-Engineered Cardiomyocyte Sheets Enhances Neovascularization and Improves Cardiac Function of Ischemic Hearts. *Circulation* **2008**, *118*, S145–152.
56. Ferrauto, G.; Castelli, D. D.; Terreno, E.; Aime, S. *In Vivo* MRI Visualization of Different Cell Populations Labeled with PARACEST Agents. *Magn. Reson. Med.* **2013**, *69*, 1703–1711.
57. Ahrens, E. T.; Flores, R.; Xu, H.; Morel, P. A. *In Vivo* Imaging Platform for Tracking Immunotherapeutic Cells. *Nat. Biotechnol.* **2005**, *23*, 983–987.
58. Hitchens, T. K.; Ye, Q.; Eytan, D. F.; Janjic, J. M.; Ahrens, E. T.; Ho, C. 19F MRI Detection of Acute Allograft Rejection with *in Vivo* Perfluorocarbon Labeling of Immune Cells. *Magn. Reson. Med.* **2011**, *65*, 1144–1153.
59. Autissier, A.; Le Visage, C.; Pouzet, C.; Chaubet, F.; Letourneur, D. Fabrication of Porous Polysaccharide-Based Scaffolds Using a Combined Freeze-Drying/Cross-Linking Process. *Acta Biomater.* **2010**, *6*, 3640–3648.
60. Le Visage, C.; Gournay, O.; Benguirat, N.; Hamidi, S.; Chaussumier, L.; Mougenot, N.; Flanders, J. A.; Isnard, R.; Michel, J. B.; Hatem, S.; *et al*. Mesenchymal Stem Cell Delivery into Rat Infarcted Myocardium Using a Porous Polysaccharide-Based Scaffold: A Quantitative Comparison with Endocardial Injection. *Tissue Eng. Part A* **2012**, *18*, 35–44.